The origin of secondary microseism Love waves

Lucia Gualtieri[a,1], Etienne Bachmann[b], Frederik J. Simons[b], and Jeroen Tromp[b,c]

[a]Department of Geophysics, Stanford University, Stanford, CA 94305-2215; [b]Department of Geosciences, Princeton University, Princeton, NJ 08544; and [c]Program in Applied & Computational Mathematics, Princeton University, Princeton, NJ 08544

Edited by Barbara A. Romanowicz, University of California, Berkeley, CA, and approved October 6, 2020 (received for review July 2, 2020)

The interaction of ocean surface waves produces pressure fluctuations at the seafloor capable of generating seismic waves in the solid Earth. The accepted mechanism satisfactorily explains secondary microseisms of the Rayleigh type, but it does not justify the presence of transversely polarized Love waves, nevertheless widely observed. An explanation for two-thirds of the worldwide ambient wave field has been wanting for over a century. Using numerical simulations of global-scale seismic wave propagation at unprecedented high frequency, here we explain the origin of secondary microseism Love waves. A small fraction of those is generated by boundary force-splitting at bathymetric inclines, but the majority is generated by the interaction of the seismic wave field with three-dimensional heterogeneity within the Earth. We present evidence for an ergodic model that explains observed seismic wave partitioning, a requirement for full-wave field ambient-noise tomography to account for realistic source distributions.

ocean–solid Earth interaction | computational seismology | seismic ambient noise | Love waves

The surface of the Earth is continuously subjected to perturbing forces that generate seismic waves. Given that 70% of the surface of our planet is covered by oceans, seismic signals due to ocean storms represent the vast majority of seismic data recorded by seismometers on Earth (1). Such data carry information about the energy exchange between different Earth systems, allowing for probing our changing climate (2–4) as well as imaging the internal structure of the Earth (5). The strongest vibrations are called secondary microseisms, excited in the 0.1 to 0.3 Hz frequency range by nonlinear ocean wave–wave interaction (6, 7). They are predominantly composed of seismic surface waves, and Rayleigh waves dominate the vertical component of microseism records (8).

The generation mechanism currently accepted for secondary microseisms explains the Rayleigh wave content of vertical-component noise records (9). Secondary microseisms are produced by pressure-like sources at the surface of the ocean. Rayleigh waves are excited below the seafloor due to constructive interference of *P* and *SV* body waves. At the ocean–crust interface, they are called Scholte waves when their phase velocity becomes smaller than the minimum phase velocity of the system (10). While at longer periods, ocean waves can directly couple with the seafloor and generate Love waves (11, 12), the generation mechanism of secondary microseisms cannot explain the presence of Love waves on the horizontal components of microseismic records. Observations of secondary microseism Love waves date back to the early (13) and middle (14) 20th century. A few recent studies based on high-quality digital data focused on quantifying the Love-to-Rayleigh ratio in the secondary microseism frequency range (*SI Appendix*, Table S1). They found that Love-to-Rayleigh ratios are frequency dependent (15) and show a predominance of Rayleigh waves (16, 17), with few exceptions (18).

Hypotheses for the generation of secondary microseism Love waves envisage that they can be generated either in the region where the pressure power spectral density (PSD) is strong or along distinct propagation paths within the Earth. The first hypothesis is supported by the presence of bathymetric inclines in the source regions. Such bathymetry may lead to splitting of the vertical second-order pressure force in a component perpendicular to inclines—responsible for Rayleigh waves—and a component tangent to inclines—responsible for Love waves. The second hypothesis is supported by the presence of lateral heterogeneities within the Earth, which can lead to the generation of Love waves due to scattering and focusing/defocusing effects. Ref. 8 observed Love and Rayleigh waves coming from the same direction, concluding that Love waves do originate in the source region. On the other hand, ref. 19 noted that the greater the distance of propagation of Rayleigh waves, the larger the Love wave energy. In addition to these hypotheses, Love waves may originate from Rayleigh-to-Love wave conversion at the ocean–continent boundary, although early numerical simulations suggest that only a few percent of incident Rayleigh wave energy can be converted to Love wave energy (20). To date, no comprehensive theoretical investigations as to which mechanisms can lead to the observed secondary microseism Love waves have been conducted.

Modeling the Generation of Secondary Microseism Love Waves

We perform global-scale, high-frequency numerical simulations using the spectral-element method (SEM) (21, 22) to assess the importance of bathymetry and three-dimensional (3D) structure on the generation of secondary microseism Love waves. The minimum period resolved by our numerical simulations is about 4 s. The SEM accommodates both 3D wave speed heterogeneities within the Earth and high-resolution bathymetry.

Significance

Secondary microseisms are the strongest background seismic vibrations of the Earth and represent the major part of global seismographic data. Secondary microseisms are generated by wind-driven ocean storms, whose energy couples with the solid Earth at the seafloor. State-of-the-art generation theories are unable to justify the presence of secondary microseism Love waves, horizontally polarized surface waves observed in two-thirds of the seismic data archive since the beginning of the 20th century. Using unprecedented high-frequency numerical simulations of global seismic wave propagation, we shed light on this 100-y-old conundrum by demonstrating that secondary microseism Love waves originate ergodically due to lateral heterogeneities in Earth structure.

Author contributions: L.G. designed the study, implemented the ambient noise sources and the computation of the rotation of the motion in SPECFEM3D_GLOBE, and performed the analysis; E.B. ported the code to GPUs and optimized the code to work on a GPU cluster at high frequency; F.J.S. and J.T. advised on the study; J.T. advised on the numerical implementation; L.G., E.B., F.J.S., and J.T. participated in the discussion of the results; and L.G. wrote the manuscript with contributions from F.J.S. and J.T.

The authors declare no competing interest.

This article is a PNAS Direct Submission.

[1]To whom correspondence may be addressed. Email: gualtieri@stanford.edu.

This article contains supporting information online at https://www.pnas.org/lookup/suppl/doi:10.1073/pnas.2013806117/-/DCSupplemental.

First published November 9, 2020.

We replace the free boundary condition at Earth's surface—the typical assumption made in seismology—by a realistic distribution of pressure point sources in the ocean, accounting for space- and frequency-dependent second-order interactions between ocean gravity waves (*Materials and Methods*) in the secondary microseism period band. We show results between 4 and 10 s. We use a source configuration in the northern hemispheric winter (*SI Appendix*, Fig. S1), when the strongest sources of secondary microseisms are located in the North Atlantic Ocean. Using the same distribution of sources, we perform numerical simulations considering either 1D Earth model PREM (Preliminary Reference Earth Model) (23) or 3D Earth model S40RTS (24) (see *Materials and Methods* for more details about the Earth models used in the numerical simulations). To assess the effect of bathymetry at the source, we use a high-resolution topography and bathymetry model (25) (*Materials and Methods*).

Fig. 1 shows the four scenarios used in our simulations: a 1D Earth model without bathymetry (Fig. 1*A*) and with bathymetry (Fig. 1*B*) and a 3D Earth model without bathymetry (Fig. 1*C*) and with bathymetry (Fig. 1*D*). In each scenario, we compute the three components of displacement due to a distribution of sources in the ocean at 199 stations worldwide (*Materials and Methods* and *SI Appendix*, Table S2).

We rotate the north–south and east–west components of displacement to the radial and transverse components by computing the rotation rate around the vertical axis at each station. This enables us to retrieve the azimuth of the main arrival at each station (26, 27) by correlating the rotation rate around the vertical axis and the transverse component of the acceleration over moving windows for varying azimuths (*Materials and Methods* and *SI Appendix*, Figs. S2–S4). This allows us to estimate the Love wave energy and the Love-to-Rayleigh energy ratio at each station. The first scenario in Fig. 1 represents the null hypothesis, where Love waves cannot be generated. We tested this case and observe that indeed no clear transversely polarized arrivals can be identified (*SI Appendix*, Figs. S2*A*–S4*A*).

Effects of Bathymetry and 3D Earth Structure

We first investigate the role played by bathymetry and/or 3D Earth structure on the generation of secondary microseism Love waves. Fig. 2 shows the power and arrival direction of Love waves in the synthetics at seismic stations around the North Atlantic Ocean, where the strongest sources of secondary microseisms are located (*SI Appendix*, Fig. S1). Background maps show the median pressure PSD (Pa^2/Hz) between about 4 and 10 s, while we use period-dependent sources in our simulations (*SI Appendix*, Fig. S1). Simulations presented in Fig. 2*A* are performed in the presence of bathymetry in 1D Earth model PREM (scenario in Fig. 1*B*). Simulations in Fig. 2*B* are performed in 3D Earth model S40RTS (scenario in Fig. 1*D*). The two scenarios allow us to compare the effects of bathymetry (Fig. 2*A*) and structure (Fig. 2*B*) on the generation of Love waves. The power of the Love waves computed at each station is proportional to the radial length of the polar histograms, while the histogram is oriented along the direction of the main arrival.

Love waves due to bathymetry and force splitting at the source (Fig. 2*A*) are nearly absent in the majority of seismic stations around the North Atlantic Ocean. We observe some larger energy at seismic stations in Europe, possibly due to the steep continental slope offshore Spain and France or the North Atlantic Ridge (*SI Appendix*, Fig. S5). The presence of Love waves at all stations dramatically increases when 3D wave speed heterogeneities are taken into account (Fig. 2*B*). This indicates that the interaction of the seismic wave field with lateral variations in Earth structure—likely through scattering and

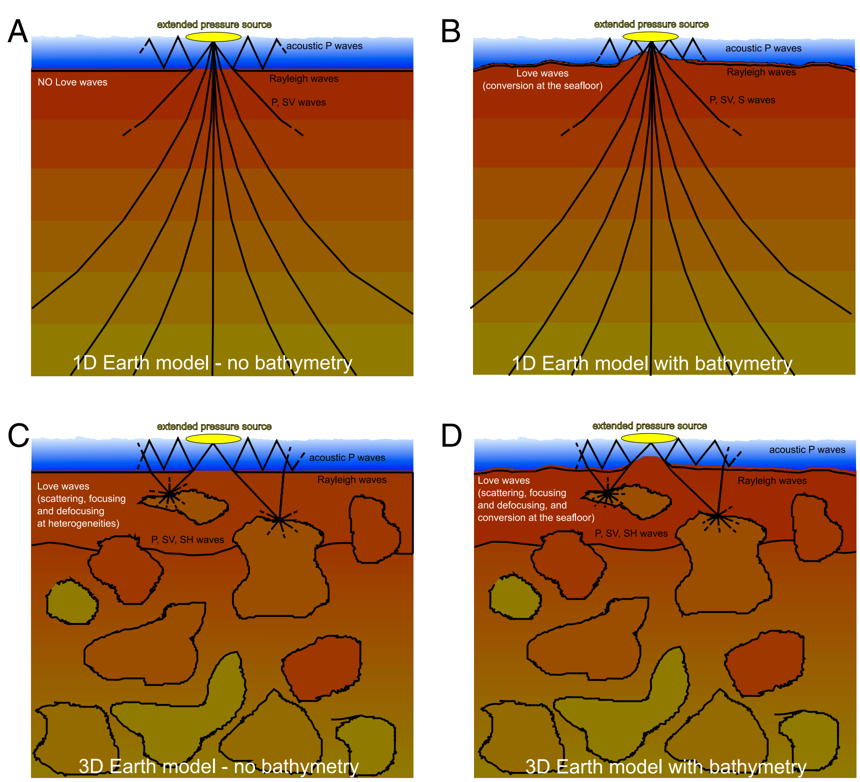

Fig. 1. The generation of secondary-microseism Love waves under various scenarios. Love waves are not generated in (*A*) a 1D Earth model without bathymetry. They do exist in the presence of (*B*) bathymetry and (*C*) 3D heterogeneity and (*D*) in a 3D Earth model with bathymetry. In this study we show that only scenario *D* comes close to explaining the hitherto unexplained observations that have been made worldwide for over a century.

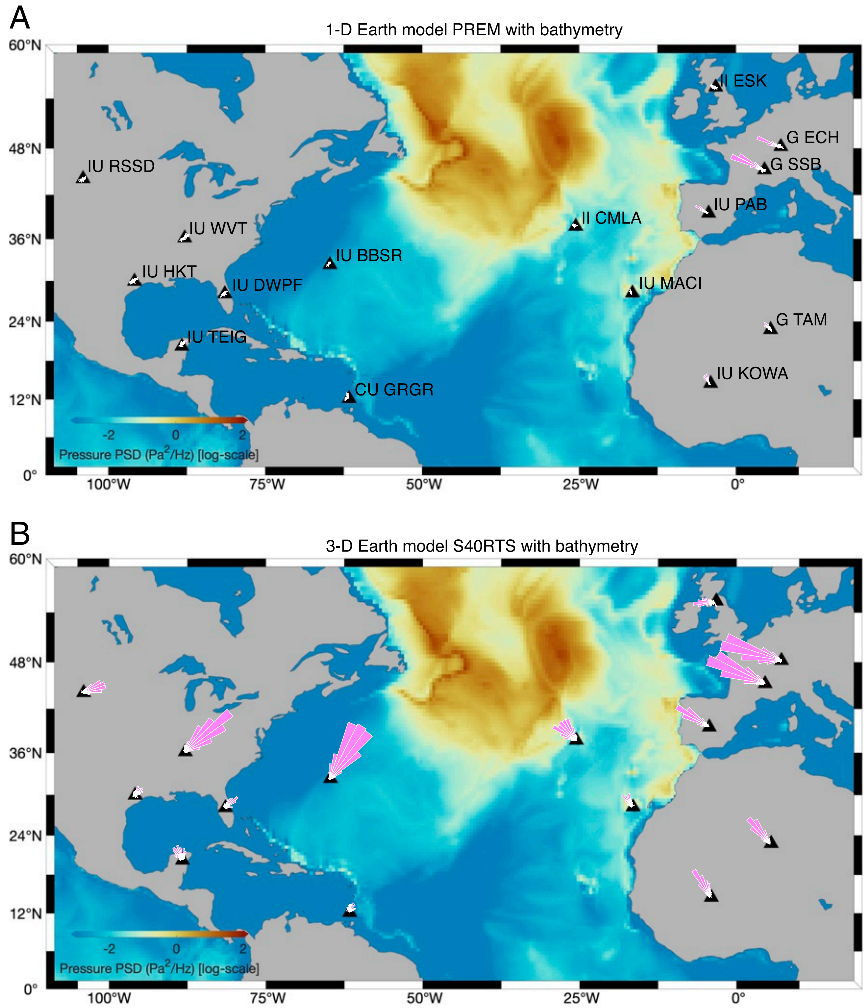

Fig. 2. Emergence of Love waves at seismic stations around the North Atlantic Ocean. Main arrival direction of secondary microseism Love waves as computed in (*A*) 1D Earth model PREM and (*B*) 3D Earth model S40RTS. The radial length of each polar histogram is proportional to the amount of Love waves at each station. In both scenarios, bathymetry is taken into account. The background color represents the median pressure PSD between periods of 4.5 and 10 s. Network and station names in *A* refer to both panels.

focusing/defocusing—yields a larger amount of secondary microseism Love waves than force splitting at the seafloor or the ocean–continent boundary. The main Love wave arrival direction at every station in Fig. 2*B* points toward the strongest source region. Therefore, the conversion from Rayleigh to Love waves occurs at depth—at heterogeneities within the Earth—in the same geographic region where the strongest sources are located. Given the smoothness of Earth model S40RTS, low-angle scattering may dominate over wide-angle scattering. The amount of Love waves (captured by the radial length of the polar histograms) is not proportional to the distance from the dominant pressure PSD, which is an indication that it is not the strength of the ocean wave–wave interaction alone that determines their generation. Rayleigh and Love wave sources have different source locations—the former are generated at the seafloor, and the latter are generated within the Earth—with important consequences for imaging methods relying on the colocation of these sources (28).

Love-to-Rayleigh Energy Ratio

We define the Love-to-Rayleigh ratio as the spectral ratio of energy on the transverse and vertical components. Fig. 3 shows the Love-to-Rayleigh spectral ratio at selected seismic stations in America, Europe, and Africa. We compare results of simulations in a 1D (blue curves) and 3D Earth models (magenta curves) in the presence of bathymetry and in a 3D Earth model in the absence of bathymetry (green curves), to assess the increase of the Love-to-Rayleigh ratio due to 3D heterogeneities. This ratio remains below 1 in most cases and exceeds 1 only at a few stations and in narrow period bands. This indicates that Rayleigh waves mostly dominate over Love waves in the secondary microseism period band, in agreement with observations (15–17). In all cases shown in Fig. 3*D*, heterogeneities (green and magenta curves) enhance the ratio toward values in the observational record. In the presence of 3D heterogeneities, bathymetry does not add any significant Love wave power (green vs. magenta curves). The 3D Earth model used in our simulations combines a 3D crustal model with a 3D mantle model (*Materials and Methods*). Crustal model Crust 2.0 accounts for two layers of sediments, as well as three layers of crust. Mantle model S40RTS captures large-scale heterogeneities but does not take into account anisotropy. Follow-up studies are needed to assess the role played by different Earth models and multiscale heterogeneities on the generation of Love waves.

Observations of the Love-to-Rayleigh ratio are extremely rare because they require arrays of stations (15, 16) or novel instruments for measuring rotational motion (18, 29). Observed values of the Love-to-Rayleigh ratio in the secondary microseism

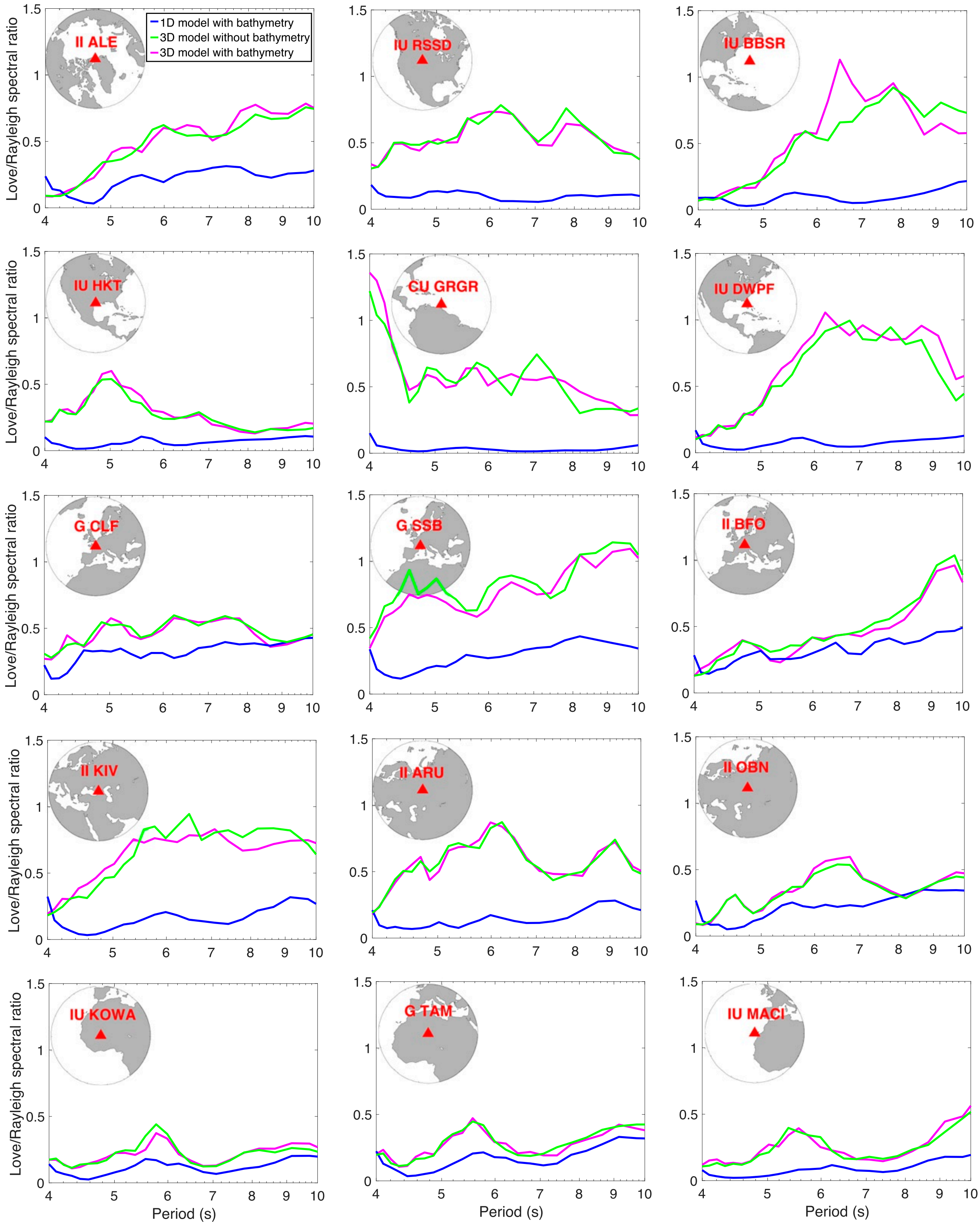

Fig. 3. Computed Love-to-Rayleigh ratio for varying periods at selected stations. Love-to-Rayleigh spectral ratio as a function of period at selected seismic stations in a 1D Earth model with bathymetry (blue curves), a 3D Earth model without bathymetry (green curves), and a 3D Earth model with bathymetry (magenta curves). Love waves are generated by bathymetry and force splitting at the source (blue curves), 3D heterogeneities within the Earth (green curves), and both mechanisms (magenta curves). *Insets* display the location of the station, while the title of each panel reflects the station name and network. The legend on the top left applies to all of the panels.

period band range from 0.25 to 1.2 (*Materials and Methods* and *SI Appendix*, Table S2). Our estimated values in the presence of 3D heterogeneities are compatible with this observed range (Fig. 3, green and magenta curves). At most stations, the presence of bathymetry alone (blue curves) underpredicts the observed ratios.

In Fig. 4 we show Love-to-Rayleigh ratios at periods of 5 s (Fig. 4*A*), 7 s (Fig. 4*B*), and 9 s (Fig. 4*C*) for seismic stations worldwide (for station locations, see *SI Appendix*, Table S2). Simulations are performed with bathymetry and 3D Earth structure (scenario in Fig. 1*D*). The background color (gray scale) reflects the pressure PSD (Pa^2/Hz) on a logarithmic scale at the corresponding period. Love-to-Rayleigh ratios are within the observed range (*Materials and Methods* and *SI Appendix*, Table S1). For all periods, stations showing the highest Love-to-Rayleigh ratios are predominantly located around the North Atlantic Ocean,

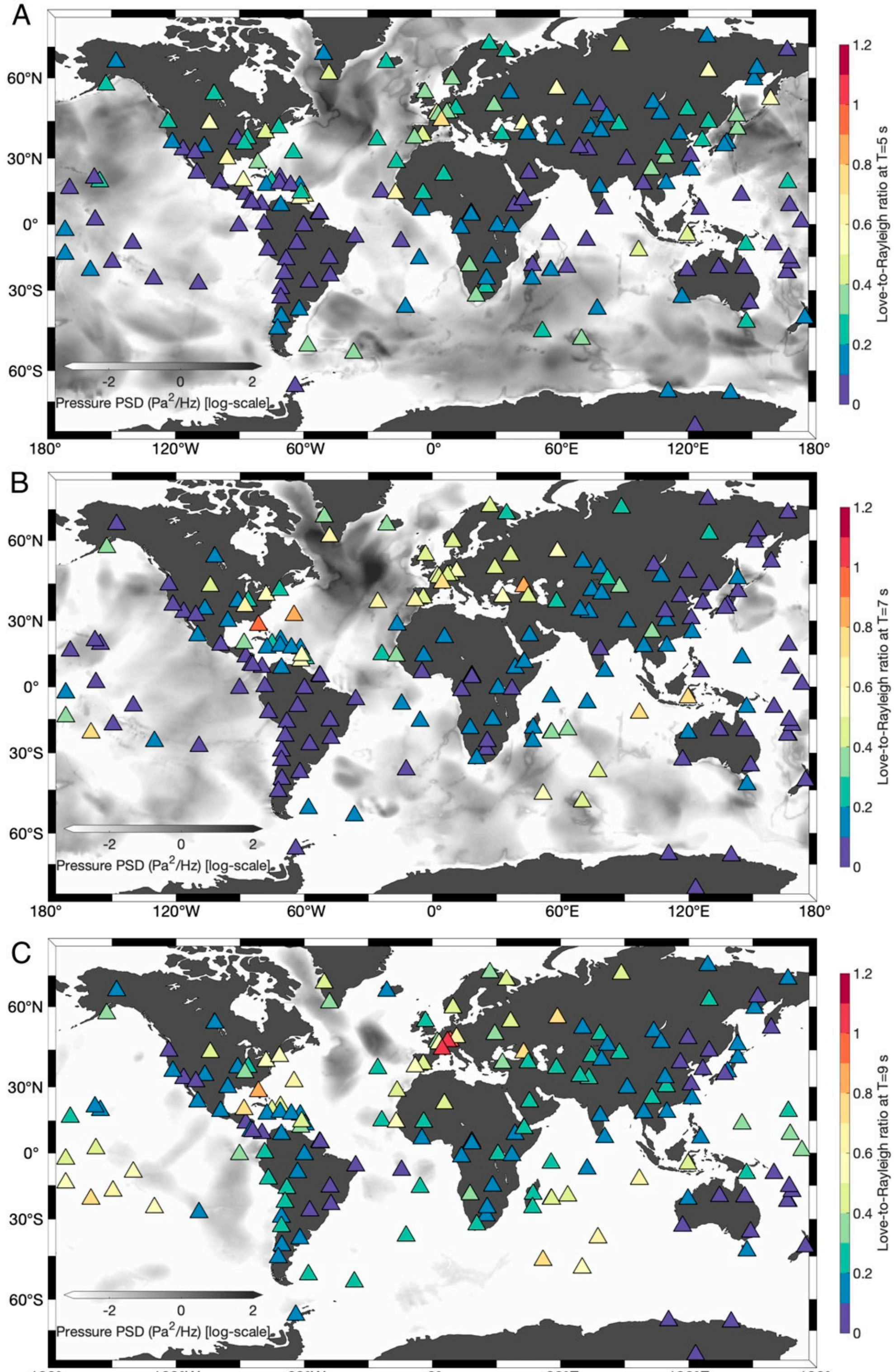

Fig. 4. Love-to-Rayleigh ratio worldwide. Love-to-Rayleigh spectral energy ratio at periods of (*A*) 5 s, (*B*) 7 s, and (*C*) 9 s. Bathymetry and 3D heterogeneities are taken into account in the simulations. The background color represents the pressure PSD at the corresponding periods.

where the sources are strongest (*SI Appendix*, Fig. S1). However, stations in the Pacific and Indian Oceans—far away from the dominant source region—show high Love-to-Rayleigh ratios that increase with increasing period. We also observe stations showing low Love-to-Rayleigh ratios, around 0.1. This occurs mostly at short periods (Fig. 4*A*) and in the southern hemisphere (Fig. 4*B*), mostly far away from strong sources. We interpret this to be an indication of the seasonal effect of sources on Love-to-Rayleigh ratios, as observed by ref. 17. Numerical simulations with seasonally varying source configurations will be required to assess the effect of storm seasonality on the generation of Love waves.

Discussion

The generation of secondary microseism Love waves has been a conundrum for close to a century (13). Attempts to locate sources of Love waves and relate them to structural or bathymetric features through numerical simulations have failed to give an explanation for their generation. For example, pioneering numerical simulations in the 1970s (20)—focusing on Rayleigh-to-Love wave conversion at the ocean continent boundary—were limited by computational power and reached 20 s as the minimum period. Recent efforts toward performing 3D numerical simulations in the secondary microseism period band—to assess the effect of 3D structure on Love wave generation—were performed at the local scale, with a Cartesian configuration, employing a single source and random-medium properties (30). Our numerical simulations of realistic global seismic wave propagation in the secondary microseism period band (4 to 10 s) reveal that lateral heterogeneities in Earth structure play a dominant role in the ergodic generation of Love waves in the seismic ambient wave field of the Earth that dominates seismic records worldwide. Force splitting at the seafloor or the ocean–continent boundary plays a smaller role.

The method used to determine the azimuth of the main arrival of secondary microseisms and compute synthetic Love-to-Rayleigh ratios (*Materials and Methods*) can also be applied to observed data. We show an example at six seismic stations in *SI Appendix*, Fig. S6. The data are compared to results of two simulations for two different mantle models, the same crustal model, and the same source configuration. Observed Love-to-Rayleigh ratios are similar to simulated ones, although we observe small differences as a function of the period. This may be due to several factors, such as the presence of signals in the data other than oceanic secondary microseisms, discrepancies of the synthetic source distribution with respect to the actual one, and small-scale heterogeneities not accounted for by the global-scale models used in the simulations. Interestingly, at some stations we observe a nonnegligible sensitivity of Love-to-Rayleigh ratios to the 3D mantle model, which needs to be investigated in future studies.

The ambient wave field recorded on horizontal-component seismograms—two-thirds of the seismic record—is often neglected in imaging studies (5). When taken into account, in the absence of information about the origin of Love waves, Rayleigh and Love waves are assumed to share the same source location, which is considered as a diffuse wave field (31). This is not the case, as Rayleigh waves arise directly from the pressure sources due to nonlinear ocean wave–wave interaction, while Love waves predominantly originate within the Earth, as shown in this study. The main arrival direction of Rayleigh and Love waves is not the same at most of the stations (*SI Appendix*, Fig. S7). Hence, seismic wave speed variations can be the result of source mislocation, leading to significant errors in models of the seismic wave speed structure of the Earth.

Our findings demonstrate that given about 30 min (*Materials and Methods* and *SI Appendix*, Fig. S8), the Earth behaves as an ergodic system under the action of heterogeneous sources in the ocean with periods between about 4 and 10 s. Starting from an initial condition—pressure sources at the ocean surface—where, even with realistic bathymetry, Love waves are not efficiently excited, the wave field evolves to a stochastic stationary state, i.e., a state containing both Love and Rayleigh waves. Any sufficiently large time periods used to assess the distribution of Love/Rayleigh wave power generated by a diffuse wave field yield similar results.

Materials and Methods

Here we describe the implementation of the 3D numerical simulations of seismic wave propagation due to a realistic diffuse secondary microseism source distribution. For figures and tables, we refer the reader to the main text as well as *SI Appendix*.

Secondary Microseism Sources. Sources of secondary microseisms are extended pressure sources at the surface of the ocean (32, 33). For computational purposes, they can be discretized on a grid of equivalent pressure point sources (6, 9). Numerical ocean wave models, such as WAVEWATCH III (34), can be used to estimate the strength of the sources. The output of the ocean wave model can be found at ftp://ftp.ifremer.fr/ifremer/ww3/HINDCAST/SISMO/ (accessed 21 May 2020).

Following refs. 7 and 35, the PSD of the pressure field at the surface of the ocean (Pa^2/ Hz) due to ocean wave–wave interaction can be written as a frequency-dependent geographical (at colatitude θ and longitude ϕ) distribution

$$F_p(f,\theta,\phi)=(2\pi)^2\,\frac{\rho_w^2\,g^2 f E^2(f_w)\,I(f_w)}{\mathrm{d}S(\theta,\phi)}, \qquad [1]$$

where ρ_w is the density of the ocean (assumed constant), g is the gravitational acceleration, and f is the frequency of the seismic waves (so that $f=2f_w$, with f_w the frequency of the water waves). Furthermore, $E(f_w)$ represents the PSD of the sea surface elevation (m^2/Hz), and $I(f_w)$ is the nondimensional ocean gravity wave energy distribution as a function of frequency, integrated over the ocean wave azimuth. The product $E^2(f_w)I(f_w)$ in Eq. **1** can be estimated using WAVEWATCH III. The elementary surface is $\mathrm{d}S=R^2\sin\theta\,\mathrm{d}\theta\,\mathrm{d}\phi$, where R is the radius of the Earth. The factor $(2\pi)^2$ enables the conversion of pressure PSD from the wavenumber domain to the spatial domain (9).

The ocean wave model is defined on a global scale with a spatial resolution of 0.5° both in latitude and in longitude. At each grid point, the ocean state is described by 24 azimuths and 22 ocean wave frequencies spaced exponentially between 0.041 Hz (24.37 s) and 0.30 Hz (3.29 s). The corresponding seismic period ranges from 1.64 to 12.18 s. One key attribute of this model is that it is the only one to date that takes into account coastal reflection of ocean waves. The amount of ocean wave energy reflected from the coast is not well constrained and should be adjusted as a function of bathymetry and shape of the coast (36). In this work, since we are ultimately interested in the ratio between Rayleigh and Love waves, we set the coastal reflection to 5% as a global average, in agreement with ref. 6.

Ocean Site Effects. In the global spectral-element solver SPECFEM3D_GLOBE (21, 22), the ocean is treated as incompressible, meaning that the entire ocean moves as a whole as a result of the normal displacement of the seafloor. The effect of the ocean on seismic wave propagation can be taken into account as a load. At long periods ($\geq$ 20 s), the thickness of the ocean is small compared with the wavelength of the seismic waves, and therefore, this is a good approximation (22). At short periods, this assumption no longer holds because the propagation of compressible (*P*) waves within the water layer has a nonnegligible effect on the seismic wave field. This is particularly important in the case of secondary microseisms, whose sources are at the ocean surface, and *P* waves generated at those sources are multiply reflected between the ocean surface and the seafloor.

The effect of the ocean on the seismic wave field in the source region (hereafter called source site effect) can be computed analytically (6), and it varies with frequency, ocean depth, and seismic phase (6, 9). Love waves are not affected by the presence of the ocean (22). This source site effect accounts for propagation within the water layer and moves the source from the top to the bottom of the ocean (9, 37, 38). The PSD of secondary microseisms is mostly dominated by surface waves. Therefore, we neglect the source site effect of body waves, and we multiply the pressure PSD in Eq. **1** by the source site effect of Rayleigh waves as computed by (6)

$$F'_p(f,\theta,\phi)=c^2(f,\theta,\phi)\,F_p(f,\theta,\phi), \qquad [2]$$

EARTH, ATMOSPHERIC, AND PLANETARY SCIENCES where $c(f, \theta, \phi)$ is the source site effect as computed by ref. 6 over the fundamental mode and the first three overtones of Rayleigh waves. This is equivalent to having a pressure source at the top of the crust and seismic waves propagating through an Earth model without an ocean (38).

SI Appendix, Fig. S1, shows examples of the frequency-varying pressure PSD at three different periods. Maps are corrected for the ocean site effect, as described by Eq. **2**.

Secondary Microseism Source Time Functions. Ocean waves can be described as the sum of many harmonics with energy at all frequencies. Since the phases of these harmonic components generally are not correlated, we consider them to be uniformly randomly distributed between 0 and 2π. Therefore, the time series of the pressure (Pa) associated with ocean wave–wave interaction at colatitude θ and longitude ϕ can be expressed in terms of a Fourier series having phase Φ:

$$P(t, \theta, \phi) = \sum_{i=1}^{N} \sqrt{2\, F_p'(f_i, \theta, \phi)\, \Delta f_i} \cos(2\pi f_i t + \Phi_i), \qquad [3]$$

where N is the number of harmonics, Δf_i is the frequency discretization of the ocean wave model, and t represents time. The factor $\sqrt{2}$ equalizes the variance of the pressure $P(t, \theta, \phi)$ to the PSD of the pressure PSD $F_p'(f, \theta, \phi)$, where $\sqrt{2}$ is the SD of uniformly distributed random cosine functions.

Sources of ambient noise are pressure fluctuations at the Earth's surface in oceanic regions. There are no ambient noise sources within the volume of the solid Earth. Therefore, computing the wave field generated by ambient noise sources corresponds to replacing the stress-free boundary condition with the nonzero ambient noise pressure source distribution.

We compute the source time function in Eq. **3** at each source defined by the ocean wave model, and we interpolate the pressure distribution across all Gauss–Lobatto–Legendre (GLL) quadrature points (see next paragraph) lying at the surface of the Earth using a bilinear interpolation. We also ensure that the total force is conserved while performing the interpolation.

Numerical Simulations. We use SPECFEM3D_GLOBE (21, 22) to perform three-component numerical simulations. Our simulations include ellipticity, self-gravitation, and the Coriolis effect. We perform 3-h-long simulations accurate down to about periods of 4 s, with 960 spectral elements along each side of a chunk in the cubed sphere. The total number of GLL points at the surface, which corresponds to the total number of sources, is 230,400.

Topography and 3D heterogeneities are switched on and off to test their effects on the generation of secondary microseism Love waves. In the absence of bathymetry, each pressure source is equivalent to a vertical point force applied to a flat surface (9). In a 1D Earth model (23), a vertical force generates *P*, *SV*, and Rayleigh waves but no shear motion (39). In the presence of bathymetry, each pressure source is equivalent to a 3D force oriented perpendicularly and parallel to the local slope. The horizontal components of the force can generate *SH* and Love waves. The presence of topography and bathymetry can also perturb the phase speed of Rayleigh and Love waves (40). The presence of 3D heterogeneities can further generate and enhance shear motion (41).

We use a smoothed version of the ETOPO2 bathymetry and topography model (25), with a resolution of 4×4 min^2 (about 7.4×7.4 km). The spatial resolution of bathymetry and topography is smaller than the minimum wavelength of seismic waves (about 12 km at $T = 4$ s considering a seismic wave speed of 3 km/s) and enables us to capture the main bathymetric features, such as the continental slope, without slowing down the computation or excessively distorting the mesh.

We perform simulations in a 1D and in a 3D Earth model. As a 1D Earth model we use the isotropic version of the spherically symmetric PREM (23). As a 3D Earth model we use S40RTS (24). When a 3D mantle model is chosen, the simulations are performed by incorporating 3D crustal model Crust2.0 (42). Crust2.0 has a resolution of $2^\circ \times 2^\circ$ (about 100×100 km), which is larger than the minimum wavelength of seismic waves considered in our simulations. Smaller-scale heterogeneities may lead to further effects on the generation of Love waves. The crustal model includes two layers of sediments (soft and hard sediments) and three layers of crust (upper, middle, and lower crust).

In the secondary microseism period band, seismic waves are mainly sensitive to the crust (43). The quality factor Q is usually tuned to get the best fit between data and synthetics (9, 44). We perform simulations with and without attenuation and verified that it does not significantly influence Love-to-Rayleigh ratios. In the results shown in this paper, the PREM radial attenuation model is incorporated as a superposition of standard linear solids (21, 45). To reduce simulation costs and scale the problem toward high frequencies, we run SPECFEM3D_GLOBE on graphics processing units (GPUs) available on the supercomputer Summit at Oak Ridge National Laboratory.

Assessing Arrival Azimuth and Estimating the Transverse Component. The transverse component of ambient noise records cannot be easily determined, since the sources are extended over a wide area, in an unknown location. As a consequence, it is not straightforward to compute the transverse component of noise records and get information about the amount of Love waves recorded at a station.

The rotational motion around the vertical axis provides a way to estimate the azimuth of the main arrival (46) and thus to compute the transverse acceleration recorded at a seismic station (26, 47), including for ambient noise (27). Assuming plane wave propagation, the amplitude of the rotation rate around the vertical axis $\dot{\omega}_z$ is proportional to the transverse acceleration a_T. The factor relating these two quantities is twice the phase velocity:

$$\frac{a_T}{\dot{\omega}_z} = -2c\,, \qquad [4]$$

where

$$\omega_z = \frac{1}{2}\left(\frac{\partial u_y}{\partial x} - \frac{\partial u_x}{\partial y}\right) \qquad [5]$$

is the rotation around the vertical axis induced by the displacement field with Cartesian components (u_x, u_y, u_z), and the overdot denotes the time derivative. The transverse acceleration and the rotation rate are in phase, meaning that the zero-lag cross-correlation coefficient between them approaches 1 during a seismic event. We use these findings to estimate the transverse acceleration a_T from the rotation ω_z computed with SPECFEM3D_GLOBE (48).

SI Appendix, Figs. S2–S4, show the emergence of Love waves at three seismic stations under the different scenarios described in Fig. 1: Fig. 1*A*, 1D Earth model PREM without bathymetry; Fig. 1*B*, 1D Earth model PREM with bathymetry; Fig. 1*C*, 3D Earth model S40RTS without bathymetry; and Fig. 1*D*, 3D Earth model S40RTS with bathymetry. *SI Appendix*, Figs. S2–S4, *Left*, show the correlation coefficient between the rotation rate around the vertical axis and all possible transverse components as a function of azimuth and time. Cross-correlations are computed over 50%-overlapping time windows. The first 2,000 s are excluded from the computation of the azimuth to avoid the nonsteady state condition (*SI Appendix*, Fig. S6). *SI Appendix*, Figs. S2–S4, *Right*, show histograms of azimuths at which the correlation coefficient exceeds 0.75.

The first scenario (*SI Appendix*, Figs. S2*A*, S3*B*, and S4*C*)—1D Earth model and absence of topography and bathymetry—represents the null hypothesis, where Love waves do not exist. We tested this case and observe that indeed no clear transverse direction of arrival can be identified. Only a small percentage of cross-correlations exceeds the threshold of 0.75.

Data Availability. SPECFEM3D_GLOBE is a freely available code through the Computational Infrastructure for Geodynamics (CIG, https://geodynamics.org/cig/software/specfem3d_globe/). The output of the ocean wave model can be found at ftp://ftp.ifremer.fr/ifremer/ww3/HINDCAST/SISMO/. Seismic data are freely available from the Data Management Center of the Incorporated Research Institutions for Seismology (IRIS). Websites were last accessed on November 3, 2020. All study data are included in the article and *SI Appendix*.

ACKNOWLEDGMENTS. We thank Congyue Cui for running numerical simulations on the supercomputer Summit at the Oak Ridge National Laboratory, Bernhard Schuberth for helping with the implementation of the rotation of the motion in SPECFEM3D_GLOBE, and Fabrice Ardhuin for making available the output of the ocean wave model. We thank the two anonymous reviewers for their comments, which greatly improved our manuscript. Plotting and data analysis made use of MATLAB. This research used resources of the Oak Ridge Leadership Computing Facility, which is a US Department of Energy Office of Science User Facility supported under contract DE-AC05-00OR22725. Additional computational resources were provided by the Princeton Institute for Computational Science & Engineering. We thank Tariq Alkhalifah and acknowledge funding from King Abdullah University of Science and Technology, grant OSR-2016-CRG5-2970-01.

1. A. Fichtner, L. Gualtieri, N. Nakata, *Seismic Ambient Noise* (Cambridge University Press, Cambridge, UK, 2019).
2. I. Grevemeyer, R. Herber, H. H. Essen, Microseismological evidence for a changing wave climate in the northeast Atlantic Ocean. *Nature* **408**, 349–352 (2000).
3. L. Gualtieri, J. S. Camargo, S. Pascale, F. M. E. Pons, G. Ekström, The persistent signature of tropical cyclones in ambient seismic noise. *Earth Planet Sci. Lett.* **484**, 287–294 (2018).
4. L. Retailleau, L. Gualtieri, Toward high-resolution period-dependent seismic monitoring of tropical cyclones. *Geophys. Res. Lett.* **46**, 1329–1337 (2019).
5. M. N. Shapiro, M. Campillo, L. Stehly, H. M. Ritzwoller, High-resolution surface-wave tomography from ambient seismic noise. *Science* **307**, 1615–1618 (2005).
6. M. S. Longuet-Higgins, A theory of the origin of microseisms. *Philos. Trans. R. Soc. A* **243**, 1–35 (1950).
7. K. Hasselmann, A statistical analysis of the generation of microseisms. *Rev. Geophys.* **1**, 177–210 (1963).
8. R. A. Haubrich, K. McCamy, Microseisms: Coastal and pelagic sources. *Rev. Geophys.* **7**, 539–571 (1969).
9. L. Gualtieri *et al.*, Modelling secondary microseismic noise by normal mode summation. *Geophys. J. Int.* **193**, 1732–1745 (2013).
10. M. A. Biot, The interaction of Rayleigh and Stoneley waves in the ocean bottom. *Bull. Seismol. Soc. Am.* **42**, 81–93 (1952).
11. Y. Fukao, K. Nishida, N. Kobayashi, Seafloor topography, ocean infragravity waves, and background Love and Rayleigh waves. *J. Geophys. Res.* **115**, B04302 (2010).
12. T. Saito, Love-wave excitation due to the interaction between a propagating ocean wave and the sea-bottom topography. *Geophys. J. Int.* **182**, 1515–1523 (2010).
13. K. Zoeppritz, Seismische Registrierungen in Göttingen im Jahre 1906. *Nachrichten von der Königlichen Gesellschaft der Wissenschaften zu Göttingen Math. Klasse* 129–190 (1908).
14. J. Darbyshire, Structure of microseismic waves: Estimation of direction of approach by comparison of vertical and horizontal components. *Philos. Trans. R. Soc. A* **223**, 96–111 (1954).
15. K. Nishida, H. Kawakatsu, Y. Fukao, K. Obara, Background Love and Rayleigh waves simultaneously generated at the Pacific Ocean floors. *Geophys. Res. Lett.* **35**, L16307 (2008).
16. A. Friedrich, F. Krüger, K. Klinge, Ocean-generated microseismic noise located with the Gräfenberg array. *J. Seismol.* **2**, 47–64 (1998).
17. T. Tanimoto *et al.*, Seasonal variations in the Rayleigh-to-Love wave ratio in the secondary microseism from colocated ring laser and seismograph. *J. Geophys. Res.* **121**, 2447–2459 (2016).
18. T. Tanimoto *et al.*, Estimate of Rayleigh-to-Love wave ratio in the secondary microseism by colocated ring laser and seismograph. *Geophys. Res. Lett.* **42**, 2650–2655 (2015).
19. H. M. Iyer, A study on the direction of arrival of microseisms at Kew Observatory. *Geophys. J. Int.* **1**, 32–43 (1958).
20. S. Gregersen, L. E. Alsop, Mode conversion of Love waves at a continental margin. *Bull. Seismol. Soc. Am.* **66**, 1855–1672 (1976).
21. D. Komatitsch, J. Tromp, Spectral-element simulations of global seismic wave propagation—I. Validation. *Geophys. J. Int.* **149**, 390–412 (2002).
22. D. Komatitsch, J. Tromp, Spectral-element simulations of global seismic wave propagation—II. Three-dimensional models, oceans, rotation and self-gravitation. *Geophys. J. Int.* **150**, 303–318 (2002).
23. A. M. Dziewonski, D. L. Anderson, Preliminary reference Earth model. *Phys. Earth Planet. In.* **25**, 297–356 (1981).
24. J. Ritsema, A. Deuss, H. J. Van Heijst, J. H. Woodhouse, S40RTS: A degree-40 shear-velocity model for the mantle from new Rayleigh wave dispersion, teleseismic traveltime and normal-mode splitting function measurements. *Geophys. J. Int.* **184**, 1223–1236 (2011).
25. National Geophysical Data Center, "2-minute gridded global relief data (ETOPO2) v2" (National Geophysical Data Center, National Oceanic and Atmospheric Administration, Washington, DC, 2006).
26. H. Igel *et al.*, Rotational motions induced by the M8. 1 Tokachi-oki earthquake, September 25, 2003. *Geophys. Res. Lett.* **32**, L08309 (2005).
27. C. Hadziioannou, P. Gaebler, U. Schreiber, J. Wassermann, H. Igel, Examining ambient noise using colocated measurements of rotational and translational motion. *J. Seismol.* **16**, 787–796 (2012).
28. T. Tanimoto, T. Yano, T. Hakamata, An approach to improve Rayleigh-wave ellipticity estimates from seismic noise: Application to the Los Angeles Basin. *Geophys. J. Int.* **193**, 407–420 (2013).
29. T. Tanimoto, C. Lin, C. Hadziioannou, H. Igel, F. Vernon, Estimate of Rayleigh-to-Love wave ratio in the secondary microseism by a small array at Piñon Flat Observatory, California. *Geophys. Res. Lett.* **43**, 11–173 (2016).
30. D. Ziane, C. Hadziioannou, The contribution of multiple scattering to Love wave generation in the secondary microseism. *Geophys. J. Int.* **217**, 1108–1122 (2019).
31. J. F. Sánchez-Sesma *et al.*, A theory for microtremor *H/V* spectral ratio: Application for a layered medium. *Geophys. J. Int.* **186**, 221–225 (2011).
32. F. Ardhuin, L. Gualtieri, E. Stutzmann, How ocean waves rock the Earth: Two mechanisms explain microseisms with periods 3 to 300 s. *Geophys. Res. Lett.* **42**, 765–772 (2015).
33. F. Ardhuin, L. Gualtieri, E. Stutzmann, "Physics of ambient noise generation by ocean waves" in *Seismic Ambient Noise*, N. Nakata, L. Gualtieri, A. Fichtner, Eds. (Cambridge University Press, Cambridge, MA, 2019), pp. 69–108.
34. L. H. Tolman, "User manual and system documentation of WAVEWATCH III (TM) version 3.14" (Tech. Rep. 276, Environmental Modeling Center, Marine Modeling and Analysis Branch, 2009),
35. F. Ardhuin, E. Stutzmann, M. Schimmel, A. Mangeney, Ocean wave sources of seismic noise. *J. Geophys. Res.* **116**, C09004 (2011).
36. F. Ardhuin, A. Roland, Coastal wave reflection, directional spread, and seismo acoustic noise sources. *J. Geophys. Res.* **117**, C00J20 (2012).
37. L. Gualtieri *et al.*, Modelling the ocean site effect on seismic noise body waves. *Geophys. J. Int.* **197**, 1096–1106 (2014).
38. V. Farra, E. Stutzmann, L. Gualtieri, M. Schimmel, F. Ardhuin, Ray-theoretical modeling of secondary microseism *P* waves. *Geophys. J. Int.* **206**, 1730–1739 (2016).
39. F. A. Dahlen, J. Tromp, *Theoretical Global Seismology* (Princeton University Press, 1998).
40. R. Snieder, The influence of topography on the propagation and scattering of surface waves. *Phys. Earth Planet. Inter.* **44**, 226–241 (1986).
41. D. Komatitsch, J. Ritsema, J. Tromp, The spectral-element method, Beowulf computing, and global seismology. *Science* **298**, 1737–1742 (2002).
42. C. Bassin, G. Laske, G. Masters, The current limits of resolution for surface wave tomography in North America. *Eos Trans. AGU* **81**, F897 (2000).
43. L. Gualtieri *et al.*, On the shaping factors of the secondary microseismic wavefield. *J. Geophys. Res.* **120**, 6241–6262 (2015).
44. E. Stutzmann, F. Ardhuin, M. Schimmel, A. Mangeney, G. Patau, Modelling long-term seismic noise in various environments. *Geophys. J. Int.* **191**, 707–722 (2012).
45. D. Komatitsch, J. Tromp, Introduction to the spectral element method for three-dimensional seismic wave propagation. *Geophys. J. Int.* **139**, 806–822 (1999).
46. H. Igel *et al.*, Broad-band observations of earthquake-induced rotational ground motions. *Geophys. J. Int.* **168**, 182–196 (2007).
47. A. Pancha, T. H. Webb, G. E. Stedman, D. P. McLeod, K. U. Schreiber, Ring laser detection of rotations from teleseismic waves. *Geophys. Res. Lett.* **27**, 3553–3556 (2000).
48. A. Cochard *et al.*, "Rotational motions in seismology: Theory, observation, simulation" in *Earthquake Source Asymmetry, Structural Media and Rotation Effects*, R. Teisseyre, E. Majewski, M. Takeo, Eds. (Springer, 2006), pp. 391–411.

PNAS
www.pnas.org

Supplementary Information for

The origin of secondary microseism Love waves

Lucia Gualtieri, Etienne Bachmann, Frederik J. Simons and Jeroen Tromp

Corresponding Author: L. Gualtieri.
E-mail: gualtieri@stanford.edu

This PDF file includes:

Supplementary text
Figs. S1 to S8
Tables S1 to S2
SI References

Supporting Information Text

Love-to-Rayleigh energy ratios reported in the literature. Recent observations based on high-quality digital data focused on quantifying Rayleigh-to-Love energy ratios in the secondary microseism period band. (1) used frequency-wavenumber analysis to locate microseisms recorded at the Gräfenberg (GRF) array in southern Germany and to estimate the energy ratio between coherent Love and Raleigh waves. They found that Rayleigh (R) waves dominate over Love (L) waves, with a ratio of $L/R = 0.25$, between periods of 6 s and 11 s. (2) applied frequency-slowness array analysis to Hi-net data in Japan and found a predominance of Rayleigh waves over Love waves with a ratio $L/R = 0.5 - 0.7$ for periods of $5 - 10$ s. (3) used a colocated ring laser and a seismometer in Wettzell, Germany, to estimate the amplitude of Love and Rayleigh waves, respectively. At periods of about 4.5 s, they found a preponderance of Love waves, and a ratio $L/R = 1.2$ in terms of kinetic energy ($L/R = 0.8$ in terms of surface amplitude). (4) further analyzed these data and revealed a seasonal pattern, with $L/R = 1.2$ throughout one year except for June and July, when Rayleigh waves dominate with $L/R = 0.8$. On the other hand, using the same technique with measurements at Piñon Flat, California, (5) found a larger proportion of Rayleigh waves all year round, with $L/R = 0.5$ at the same frequencies as (3). Employing a beamforming analysis for several arrays in Europe, (6) found that L/R varies with location and season between 0.4 and 1.2.

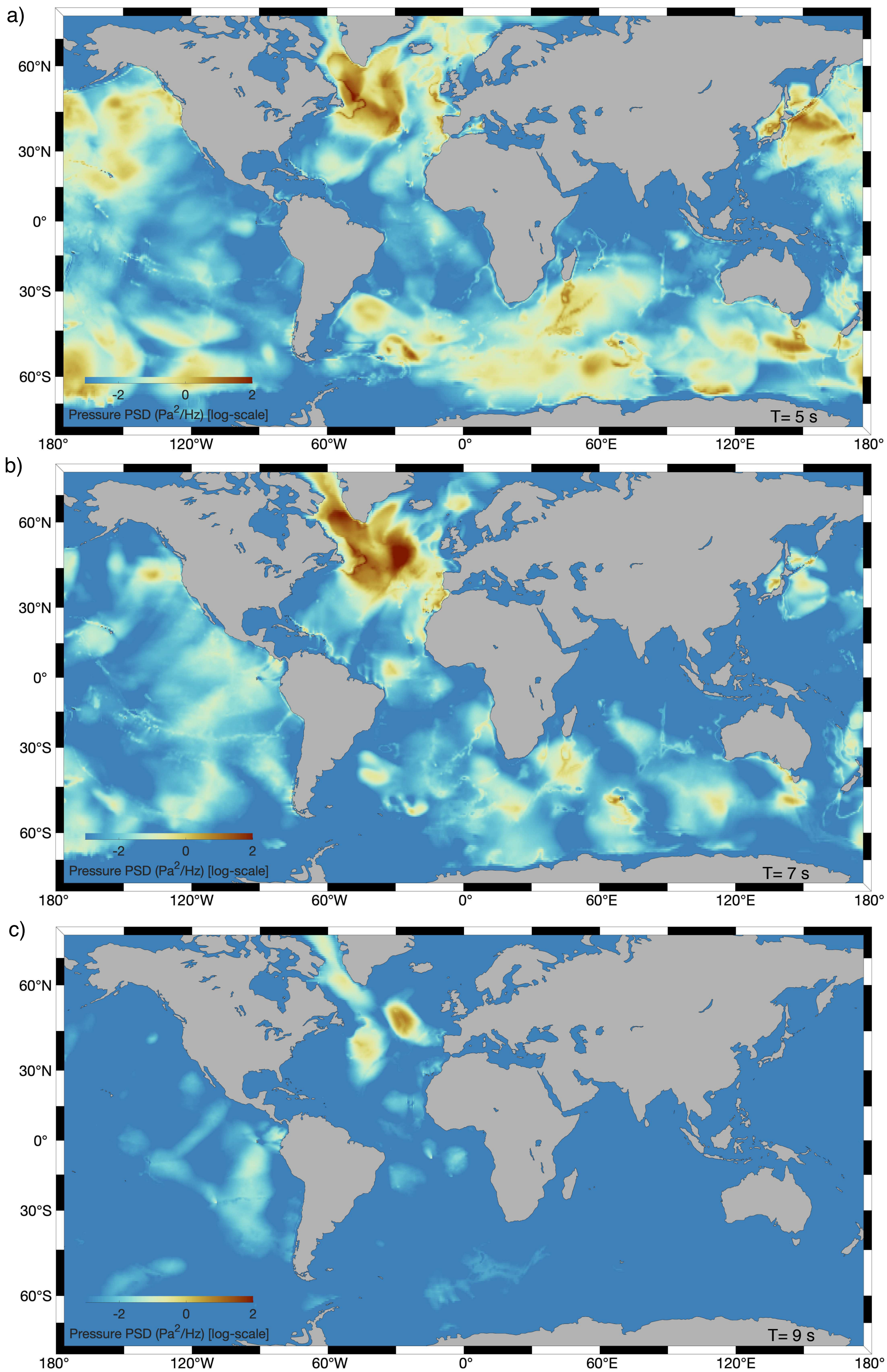

Fig. S1. Sources of secondary microseisms for varying periods. Three examples of pressure PSD (Pa^2 / Hz, log scale) on January 1, 2010, at periods of (a) 5 s, (b) 7 s, and (c) 9 s. Our source time functions account for the frequency-varying PSD defined by the ocean wave model.

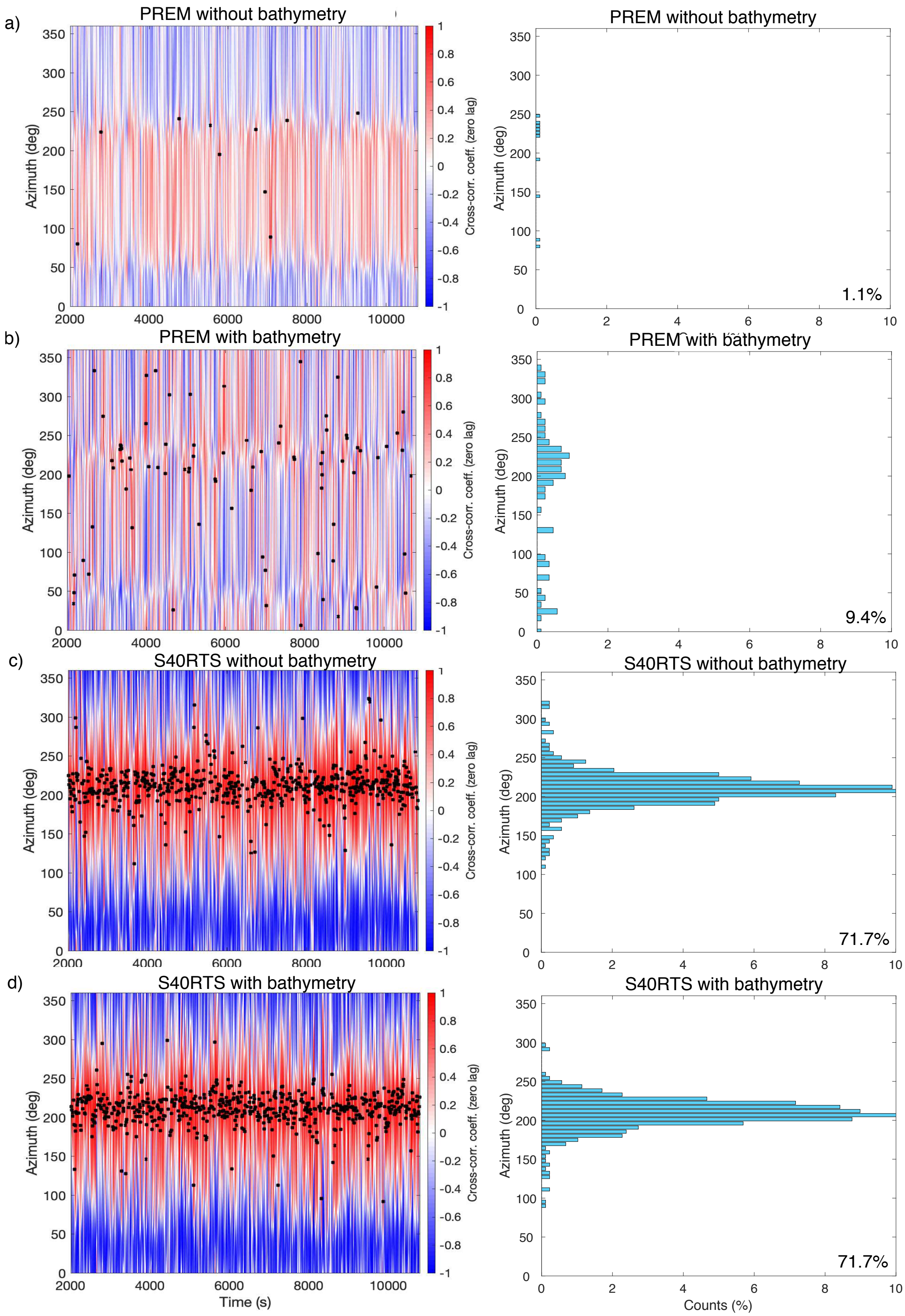

Fig. S2. Emergence of Love waves in various scenarios. Simulations at station BBSR (St George's, Bermuda) performed in PREM (a) without bathymetry and (b) with bathymetry, and S40RTS (c) without bathymetry and (d) with bathymetry. Left: cross-correlation between rotation rate around the vertical axis and all possible transverse components as a function of azimuth and time. Black crosses denote cross-correlation values larger than 0.75. Right: histograms of cross-correlation values exceeding 0.75. The overall sum percentage is shown in the bottom right-hand corner of each figure.

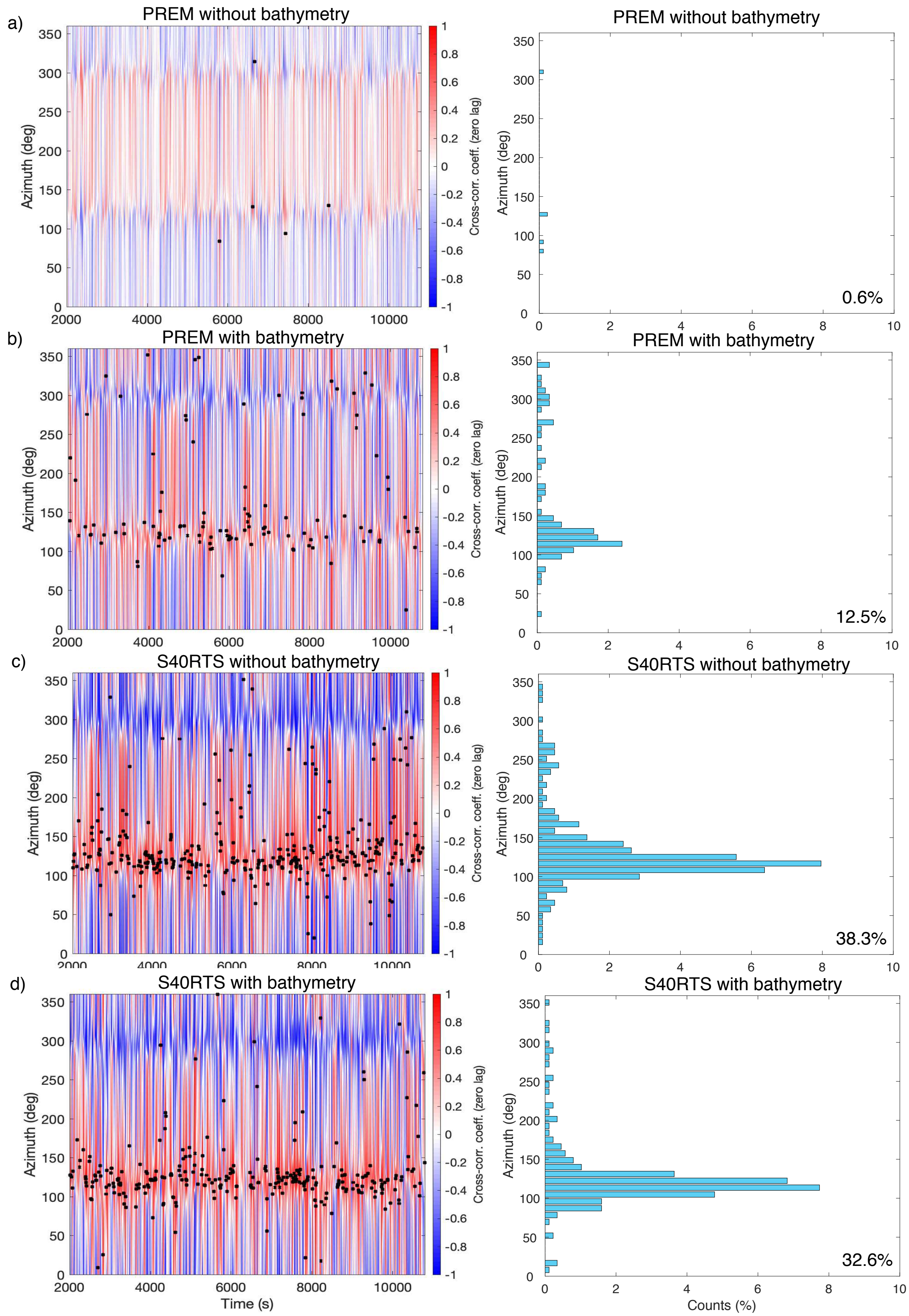

Fig. S3. Emergence of Love waves in various scenarios. Same as in Figure S2, but for station PAB (San Pablo, Spain).

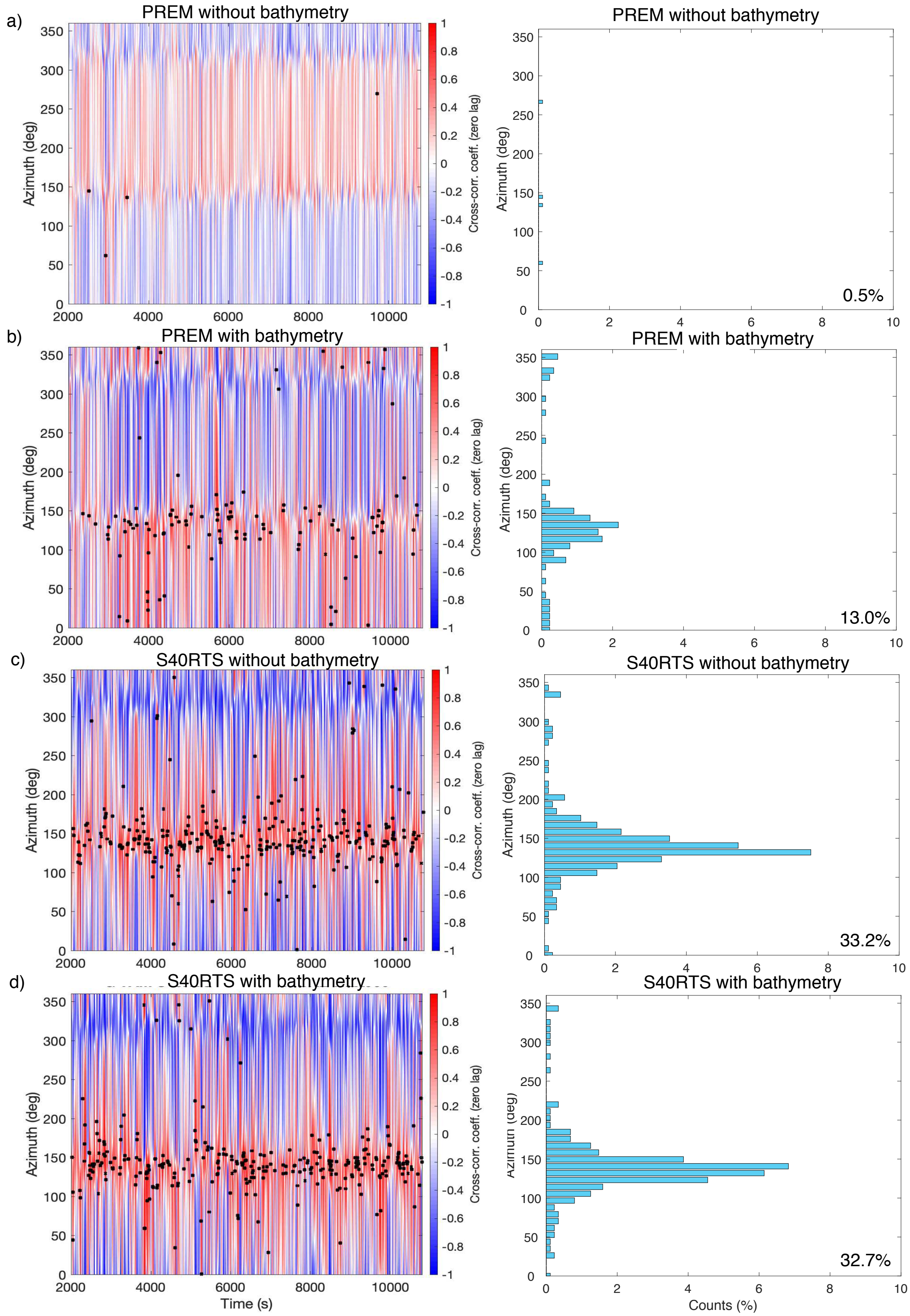

Fig. S4. Emergence of Love waves in various scenarios. Same as in Figure S2, but for station TAM (Tamanrasset, Algeria).

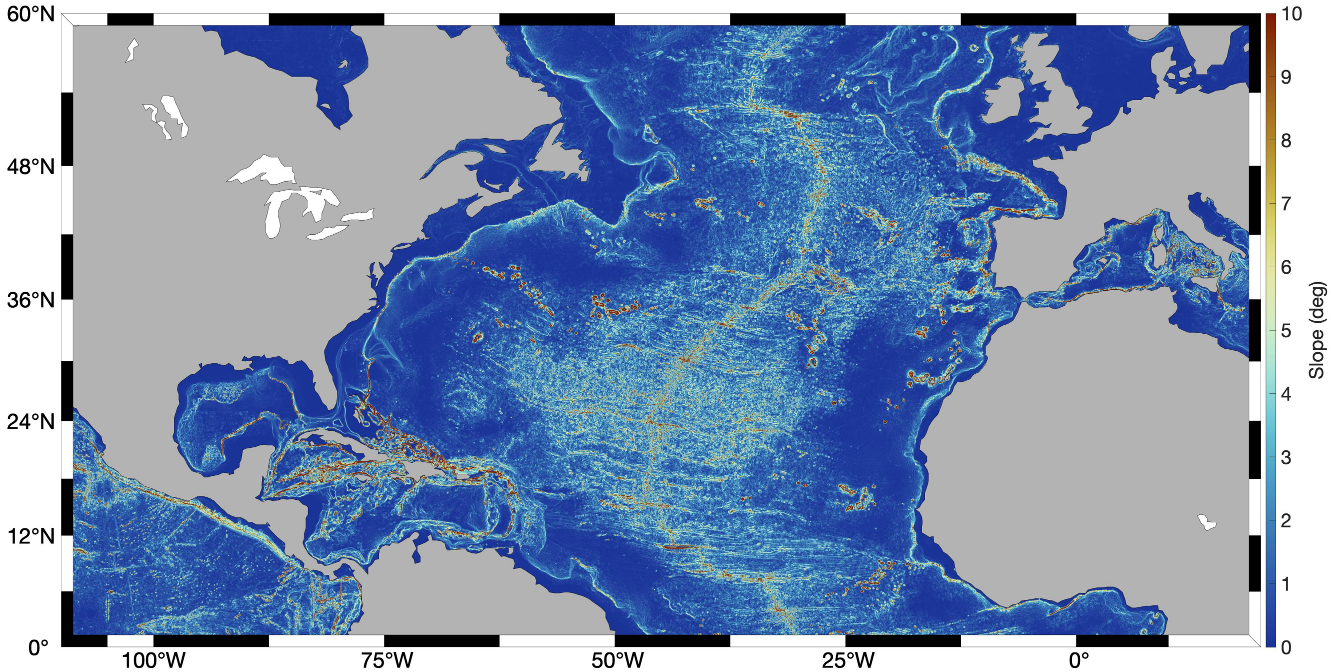

Fig. S5. Slope of the seafloor in the North Atlantic Ocean. The horizontal force due to force splitting at the seafloor responsible for the generation of Love waves is proportional to the sine of the slope.

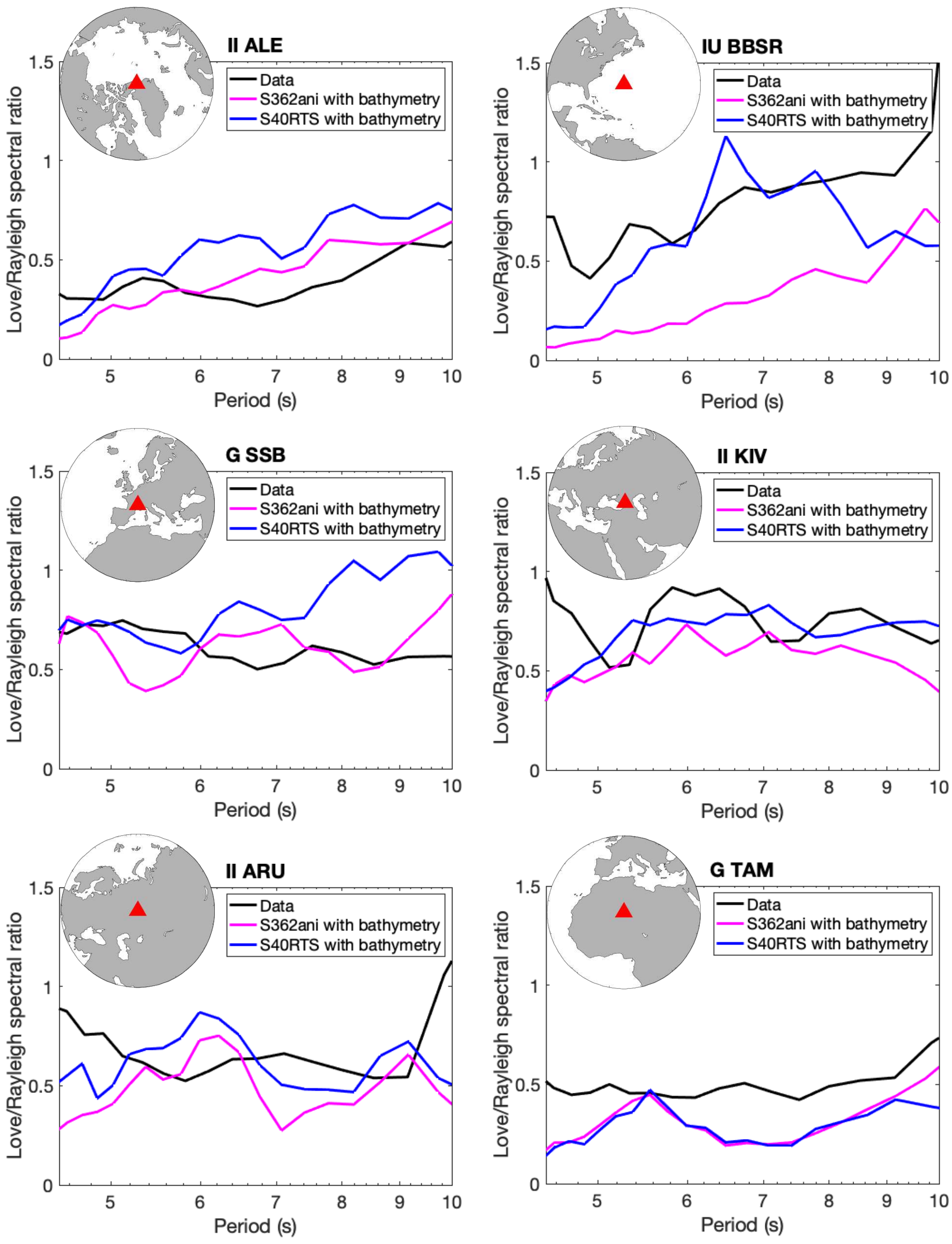

Fig. S6. Observed *versus* simulated Love-to-Rayleigh ratios. Comparison between observed (black) and synthetic (blue and magenta) Love-to-Rayleigh ratios at six seismic stations in Fig. 3. Synthetic data are computed considering two different mantle models: S40RTS (7) and S362ANI (8).

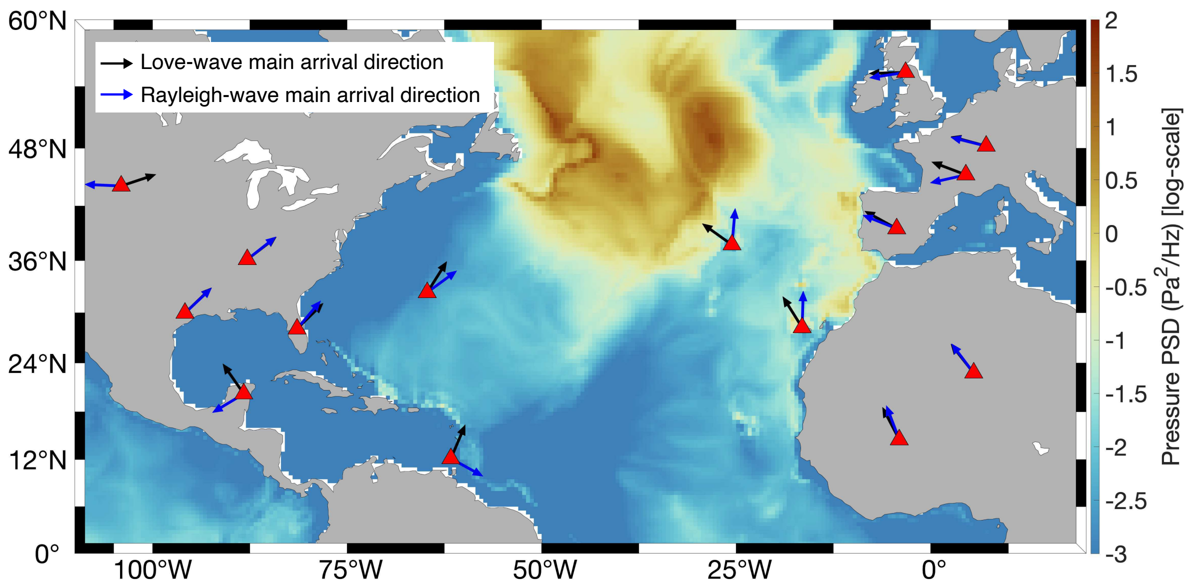

Fig. S7. Comparison between the main direction of arrival of Love and Rayleigh waves. The main direction of arrival of Rayleigh waves has been estimated by finding the location at which the source in equation (1) (Materials and Methods), scaled by a factor that accounts for the propagation of Rayleigh waves, is maximum. The Rayleigh-wave propagation factor is defined as $[\exp((-\omega\Delta R)/(Q\,U))]/[R\,\sin(\Delta)]$, where Δ is the spherical distance between every source and each station, R is the radius of the Earth, Q is the quality factor—assumed constant and equal to the PREM value at the surface ($Q = 600$), and U is the group speed of the fundamental mode of Rayleigh waves. Scattering effects on Rayleigh waves are not taken into account, as it has been shown that the direct wavefield suffices for modeling vertical-component secondary microseisms, and thus to estimate the Raylegh-wave content at each station (e.g. 9, 10). The main Love wave arrival direction is estimated as described in Materials and Methods using 3D Earth model S40RTS with bathymetry and corresponds to what is shown in Figure 2b. At most of the stations, Rayleigh and Love waves do not share the same direction of arrival.

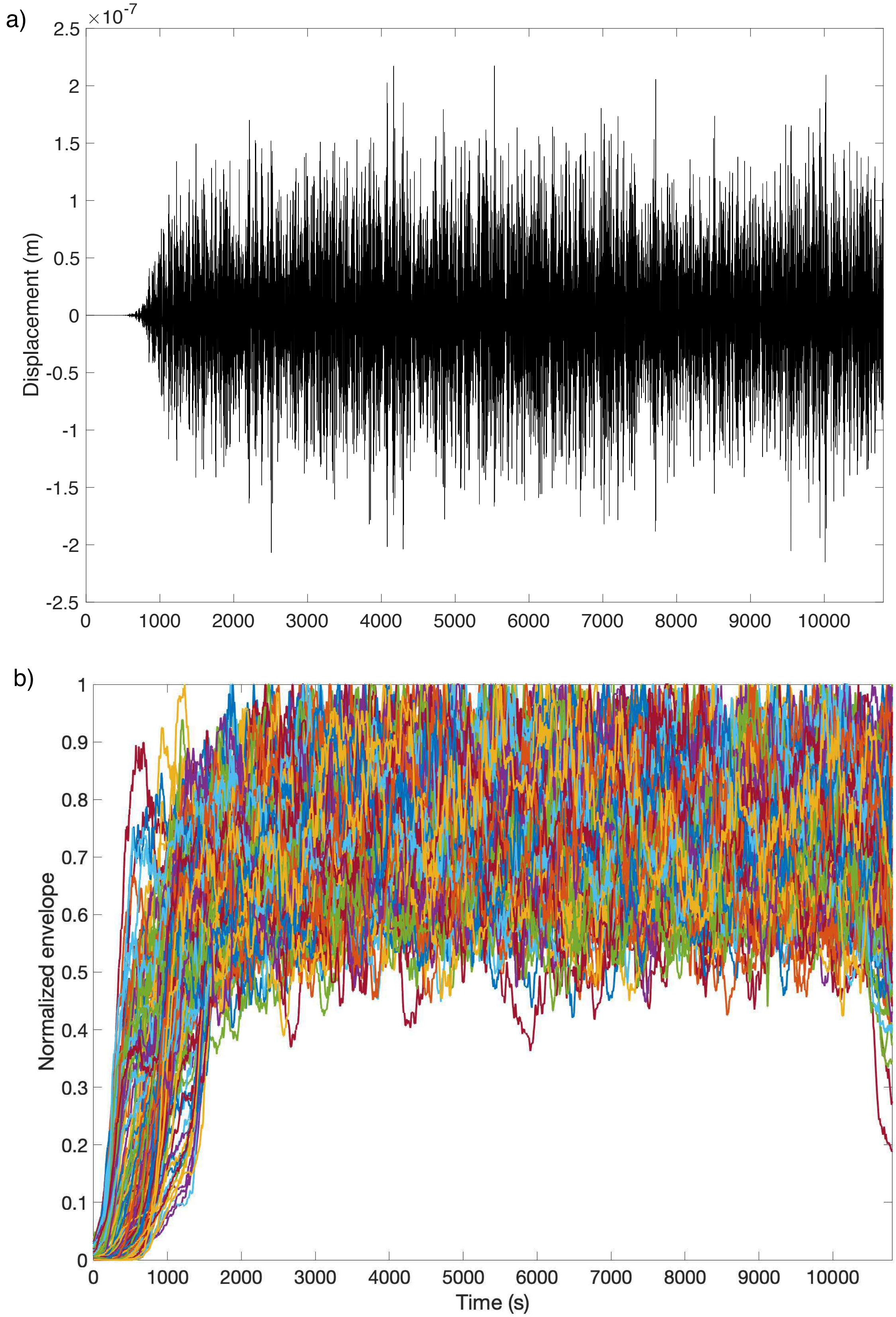

Fig. S8. Time to reach steady-state conditions. (a) Example of synthetic vertical-component seismogram at one station. (b) Envelope of all vertical-component synthetic seismograms as a function of time. Each colored line refers to one of the 199 seismic stations employed in this study, normalized by its maximum amplitude. We applied a moving median over time windows of 5 minutes to slightly smooth the curves. Steady-state conditions are reached after about 30 min.

Table S1. Love-to-Rayleigh energy ratios reported in the literature.

Publication	Location	Period band (s)	Love-to-Rayleigh energy ratio
(1)	Gräfenberg array (Germany)	6–11	0.25
(2)	Hi-net (Japan)	5–10	0.5–0.7
(3)	Wettzell (Germany)	4.5	1.2
(5)	Wettzell (Germany)	4.5	0.8–1.2
(4)	Piñon Flat (California)	4.5	0.5
(6)	several locations in Europe	5–10	0.4–1.2

Table S2. Seismic stations used in the numerical simulations. Stations shown in Figures 2 and 3 in the main text are shown in bold font. More information about stations can be found at https://www.fdsn.org.

Station	Network	Latitude (deg)	Longitude (deg)
ANWB	CU	17.6690	-61.7860
BBGH	CU	13.1430	-59.5590
BCIP	CU	9.1660	-79.8370
GRGR	**CU**	**12.1320**	**61.6540**
GRTK	CU	21.5110	-71.1330
GTBY	CU	19.9270	-75.1110
MTDJ	CU	18.2260	-77.5350
SDDR	CU	18.9820	-71.2880
TGUH	CU	14.0570	-87.2730
BDFB	GT	-15.6420	-48.0150
BGCA	GT	5.1760	18.4240
BOSA	GT	-28.6140	25.2560
CPUP	GT	-26.3310	-57.3310
DBIC	GT	6.6700	-4.8570
LBTB	GT	-25.0150	25.5970
LPAZ	GT	-16.2880	-68.1310
PLCA	GT	-40.7330	-70.5510
VNDA	GT	-77.5170	161.8530
BJT	IC	40.0180	116.1680
ENH	IC	30.2760	109.4940
HIA	IC	49.2700	119.7410
KMI	IC	25.1230	102.7400
LSA	IC	29.7030	91.1270
MDJ	IC	44.6170	129.5910
QIZ	IC	19.0290	109.8440
SSE	IC	31.0950	121.1910
WMQ	IC	43.8140	87.7050
XAN	IC	34.0310	108.9240
AAK	II	42.6390	74.4940
ABKT	II	37.9300	58.1190
ABPO	II	-19.0180	47.2290
ALE	**II**	**82.5030**	**-62.3500**
ARU	**II**	**56.4300**	**58.5620**
ASCN	II	-7.9330	-14.3600
BFO	**II**	**48.3320**	**8.3310**
BORG	II	64.7470	-21.3270
BRVK	II	53.0580	70.2830
CMLA	**II**	**37.7640**	**-25.5240**
COCO	II	-12.1900	96.8350
DGAR	II	-7.4120	72.4530
EFI	II	-51.6750	-58.0640
ERM	II	42.0150	143.1570
ESK	**II**	**55.3170**	**-3.2050**
FFC	II	54.7250	-101.9780
HOPE	II	-54.2840	-36.4880
JTS	II	10.2910	-84.9530
KAPI	II	-5.0140	119.7520
KDAK	II	57.7830	-152.5830
KIV	**II**	**43.9550**	**42.6860**
KURK	II	50.7150	78.6200
KWAJ	II	8.8020	167.6130
LVZ	II	67.8980	34.6510
MBAR	II	-0.6020	30.7380
MSEY	II	-4.6740	55.4790
MSVF	II	-17.7450	178.0530
NIL	II	33.6510	73.2690
NNA	II	-11.9880	-76.8420
NRIL	II	69.5050	88.4410

OBN	**II**	**55.1150**	**36.5670**
PALK	II	7.2730	80.7020
PFO	II	33.6110	-116.4560
RAYN	II	23.5230	45.5030
RPN	II	-27.1270	-109.334
SACV	II	14.9700	-23.6080
SHEL	II	-15.9590	-5.7460
SUR	II	-32.3800	20.8120
TAU	II	-42.9100	147.3200
TLY	II	51.6810	103.6440
WRAB	II	-19.9340	134.3600
ADK	IU	51.8820	-176.6840
AFI	IU	-13.9090	-171.7770
ANMO	IU	34.9460	-106.4570
ANTO	IU	39.8680	32.7930
BBSR	**IU**	**32.3710**	**-64.6960**
BILL	IU	68.0650	166.4530
CASY	IU	-66.2790	110.5350
CCM	IU	38.0560	-91.2450
CHTO	IU	18.8140	98.9440
COLA	IU	64.8740	-147.8620
COR	IU	44.5860	-123.3050
CTAO	IU	-20.0880	146.2550
DAV	IU	7.0700	125.5790
DWPF	**IU**	**28.1100**	**-81.4330**
FUNA	IU	-8.5260	179.1970
FURI	IU	8.8950	38.6800
GNI	IU	40.1480	44.7410
GRFO	IU	49.6910	11.2200
GUMO	IU	13.5890	144.8680
HKT	**IU**	**29.9620**	**-95.8380**
HNR	IU	-9.4390	159.9470
HRV	IU	42.5060	-71.5580
INCN	IU	37.4780	126.6240
JOHN	IU	16.7330	-169.5290
KBL	IU	34.5410	69.0430
KBS	IU	78.9150	11.9380
KEV	IU	69.7570	27.0030
KIEV	IU	50.7010	29.2240
KIP	IU	21.4200	-158.0110
KMBO	IU	-1.1270	37.2520
KNTN	IU	-2.7740	-171.7190
KONO	IU	59.6490	9.5980
KOWA	**IU**	**14.4970**	**-4.0140**
LCO	IU	-29.0110	-70.7000
LSZ	IU	-15.2780	28.1880
LVC	IU	-22.6130	-68.9110
MA2	IU	59.5760	150.7700
MACI	**IU**	**28.2500**	**-16.5080**
MAJO	IU	36.5460	138.2040
MAKZ	IU	46.8080	81.9770
MBWA	IU	-21.1590	119.7310
MIDW	IU	28.2160	-177.3700
MSKU	IU	-1.6560	13.6120
NWAO	IU	-32.9280	117.2390
OTAV	IU	0.2380	-78.4510
PAB	**IU**	**39.5450**	**-4.3500**
PAYG	IU	-0.6740	-90.2860
PET	IU	53.0230	158.6500
PMG	IU	-9.4050	147.1600
PMSA	IU	-64.7740	-64.0490

POHA	IU	19.7570	-155.5330
PTCN	IU	-25.0710	-130.0950
PTGA	IU	-0.7310	-59.9670
QSPA	IU	-89.9290	144.4380
RAO	IU	-29.2450	-177.9290
RAR	IU	-21.2120	-159.7730
RCBR	IU	-5.8270	-35.9010
RSSD	**IU**	**44.1210**	**-104.036**0
SAML	IU	-8.9490	-63.1830
SBA	IU	-77.8490	166.7570
SDV	IU	8.8840	-70.6340
SFJD	IU	66.9960	-50.6210
SJG	IU	18.1090	-66.1500
SLBS	IU	23.6860	-109.9440
SNZO	IU	-41.3090	174.7040
SSPA	IU	40.6360	-77.8880
TARA	IU	1.3550	172.9230
TATO	IU	24.9740	121.4970
TEIG	**IU**	**20.2260**	**-88.2760**
TIXI	IU	71.6340	128.8670
TRIS	IU	-37.0680	-12.3150
TRQA	IU	-38.0570	-61.9790
TSUM	IU	-19.2020	17.5840
TUC	IU	32.3100	-110.7850
ULN	IU	47.8650	107.0530
WAKE	IU	19.2830	166.6520
WCI	IU	38.2290	-86.2940
WVT	**IU**	**36.1300**	**-87.8300**
XMAS	IU	2.0450	-157.4460
YAK	IU	62.0310	129.6800
YSS	IU	46.9590	142.7600
AGD	G	11.5290	42.8240
AIS	G	-37.7964	77.5692
ATD	G	11.5307	42.8466
BNG	G	4.4350	18.5470
CAN	G	-35.3187	148.9963
CAY	G	4.9480	-52.3170
CCD	G	-75.1065	123.3050
CLF	**G**	**48.0258**	**2.2600**
COYC	G	-45.5730	-72.0814
CRZF	G	-46.4310	51.8553
DRV	G	-66.6649	140.0021
DZM	G	-22.0716	166.4438
ECH	**G**	**48.2163**	**7.1590**
EVO	G	38.5320	-8.0130
FDF	G	14.7350	-61.1463
FOMA	G	-24.9757	46.9789
FUTU	G	-14.3077	-178.1211
GRC	G	47.2955	3.0736
HDC	G	10.0020	-84.1114
HDC2	G	10.0270	-84.1170
HYB	G	17.4187	78.5521
INU	G	35.3500	137.0290
IVI	G	61.2058	-48.1712
KIP	G	21.4200	-158.0112
KOG	G	5.2070	-52.7320
MBO	G	14.3920	-16.9555
MPG	G	5.1101	-52.6445
NOC	G	-22.2840	166.4320
NOUC	G	-22.0986	166.3067
PAF	G	-49.3510	70.2107

PCR	G	-21.2084	55.5721
PEL	G	-33.1436	-70.6749
PPT	G	-17.5690	-149.5760
PPTF	G	-17.5896	-149.5653
PVC	G	-17.7400	168.3120
RER	G	-21.1712	55.7399
ROCAM	G	-19.7555	63.3701
RODM	G	-19.6962	63.4413
SANVU	G	-15.4471	167.2032
SCZ	G	36.5980	-121.4048
SEY	G	62.9330	152.3730
SPB	G	-23.5927	-47.4270
SSB	**G**	**45.2790**	**4.5420**
TAM	**G**	**22.7915**	**5.5284**
TAOE	G	-8.8549	-140.1478
TRIS	G	-37.0681	-12.3152
UNM	G	19.3297	-99.1781
WFM	G	42.6110	-71.4910
WUS	G	41.2007	79.2165

References

1. A Friedrich, F Krüger, K Klinge, Ocean-generated microseismic noise located with the Gräfenberg array. *J. Seismol.* **2**, 47–64 (1998).
2. K Nishida, H Kawakatsu, Y Fukao, K Obara, Background Love and Rayleigh waves simultaneously generated at the Pacific Ocean floors. *Geophys. Res. Lett.* **35**, L16307 (2008).
3. T Tanimoto, et al., Estimate of Rayleigh-to-Love wave ratio in the secondary microseism by colocated ring laser and seismograph. *Geophys. Res. Lett.* **42**, 2650–2655 (2015).
4. T Tanimoto, et al., Seasonal variations in the Rayleigh-to-Love wave ratio in the secondary microseism from colocated ring laser and seismograph. *J. Geophys. Res.* **121**, 2447–2459 (2016).
5. T Tanimoto, C Lin, C Hadziioannou, F Igel, Hand Vernon, Estimate of Rayleigh-to-Love wave ratio in the secondary microseism by a small array at Piñon Flat Observatory, California. *Geophys. Res. Lett.* **43**, 11–173 (2016).
6. C Juretzek, C Hadziioannou, Where do ocean microseisms come from? A study of Love-to-Rayleigh wave ratios. *J. Geophys. Res.* **121**, 6741–6756 (2016).
7. J Ritsema, A Deuss, HJ Van Heijst, JH Woodhouse, S40RTS: a degree-40 shear-velocity model for the mantle from new Rayleigh wave dispersion, teleseismic traveltime and normal-mode splitting function measurements. *Geophys. J. Int.* **184**, 1223–1236 (2011).
8. B Kustowski, G Ekström, A Dziewoński, Anisotropic shear-wave velocity structure of the Earth's mantle: A global model. *J. Geophys. Res. Solid Earth* **113** (2008).
9. E Stutzmann, F Ardhuin, M Schimmel, A Mangeney, G Patau, Modelling long-term seismic noise in various environments. *Geophys. J. Int.* **191**, 707–722 (2012).
10. L Gualtieri, et al., Modelling secondary microseismic noise by normal mode summation. *Geophys. J. Int.* **193**, 1732–1745 (2013).